ISSN 1063-7745, Crystallography Reports, 2018, Vol. 63, No. 1, pp. 37–44. © Pleiades Publishing, Inc., 2018.
Original Russian Text © A.P. Dudka, A.M. Balbashov, 2018, published in Kristallografiya, 2018, Vol. 63, No. 1, pp. 43–51.

STRUCTURE OF INORGANIC COMPOUNDS

Structural Analysis of $Sr_3NbFe_3Si_2O_{14}$ Single Crystal from the Langasite Family and Finding of Negative Thermal Expansion in the Range of 83–110 K

A. P. Dudka[a,*] and A. M. Balbashov[b]

[a] *Shubnikov Institute of Crystallography, Federal Scientific Research Centre "Crystallography and Photonics," Russian Academy of Sciences, Moscow, 119333 Russia*

[b] *National Research University MPEI, Moscow, 111250 Russia*

**e-mail: dudka@ns.crys.ras.ru*

Received February 1, 2017

Abstract—Iron-containing $Sr_3NbFe_3Si_2O_{14}$ single crystals from the langasite family, which are interesting for researchers due to their magnetic ordering at $T_N = 26$ K, have been grown by the floating zone melting method. Accurate X-ray diffraction analysis is performed at 293 and 90.5 K using the data collected on a CCD diffractometer. To compensate for systematic errors, two data sets are collected at each temperature. The structure is refined based on averaged data set: sp. gr. $P321$, $Z = 1$, $\sin\theta/\lambda \le 1.35$ Å^{-1}; $a = 8.2609(4)$ Å, $c = 5.1313(3)$ Å at 293 K and $a = 8.2344(6)$ Å, $c = 5.1243(6)$ Å at 90.5 K; the agreement factors are $R/wR =$ 1.18/1.03% and $\Delta\rho_{min}/\Delta\rho_{max} = -0.57/0.25$ e/Å^3 for 3583 independent reflections at 293 K and $R/wR =$ 1.18/1.13% and $\Delta\rho_{min}/\Delta\rho_{max} = -0.54/0.23$ e/Å^3 for 3638 reflections at 90.5 K. Negative thermal expansion in the direction of the cell c axis is revealed in the range of 83–110 K.

DOI: 10.1134/S1063774518010066

INTRODUCTION

$Sr_3NbFe_3Si_2O_{14}$ (SNFS) crystals belong to the vast langasite family ($Ca_3Ga_2Ge_4O_{14}$ structure type, sp. gr. $P321$, $Z = 1$ [1]). Its representatives are characterized by a variety of physical properties, among which piezoelectric effect has been most demanded for a long time [2]. The abbreviation SNFS indicates to four cations occupying Wyckoff positions 3*e* (Sr, symmetry axis 2), 1*a* (Nb, intersection of symmetry axes 3 and 2), 3*f* (Fe, symmetry axis 2), and 2*d* (Si, symmetry axis 3) in the unit cell. The three independent 2*d* sites (symmetry axis 3), 6*g* (general site), and 6*g* are occupied by oxygen atoms (Fig. 1).

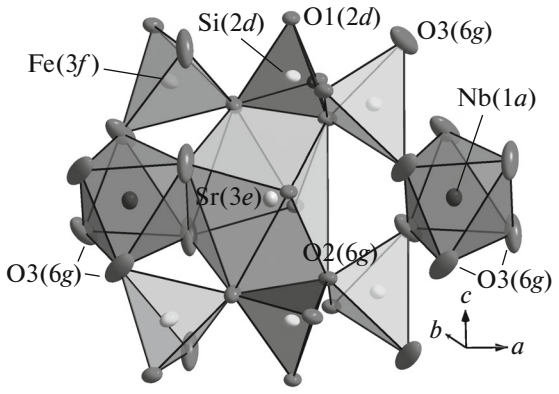

Fig. 1. Polyhedral representation of the $Sr_3NbFe_3Si_2O_{14}$ structure.

The magnetic properties of the compounds belonging to this family have actively been investigated in the last years [3, 4]. Crystals containing magnetic ions in the 3*f* site exhibit magnetic ordering at the Neel temperature $T_N \approx 30$ K [5, 6]. This effect, revealed in crystals possessing electric polarization under certain conditions [7], makes them promising multiferroics [8]. Magnetic ordering occurs along a helix, consisting of magnetic ions in the 3*f* site [8] and oxygen atoms in the general site 6*g*, which are bound by indirect exchange interaction [6].

The magnetic helix has an immediate structural base, despite the fact that the sp. gr. $P321$ does not contain screw symmetry axes. This base (structural helix) is formed by the electron density of the cations in the 3*f* site and anions O3(6*g*) [9, 10]. Moreover, the atomic sites forming the helix are split, and the atoms exhibit preferred displacements along the helix line even at room and liquid nitrogen temperatures, as a result of which the effective interatomic distances are reduced and the interatomic interaction is enhanced [11, 12]. The helix twist direction, which determines the crystal chirality (right- or left-handed), must be taken into account in the design of data storage devices.

Along with X-ray diffraction studies, splitting of the 3*f* site at $T < T_N$ was revealed in the Mossbauer investigation of Fe^{3+} multiferroics [5, 13]. A spread in the local atomic environment was also observed in the NMR spectroscopy of $Nd_3Ga_5SiO_{14}$ compound [14]. Structural data on 19 crystals belonging to the langasite family indicate disordering of atomic sites, both in crystals having mixed atomic sites ($Ca_3Ga_2Ge_4O_{14}$ [9], $Nd_3Ga_5SiO_{14}$ [10], $La_3Ga_5SiO_{14}$ [11], $La_3Ga_5GeO_{14}$ [12]) and in crystals without such sites ($Ca_3TaGa_3Si_2O_{14}$ [15], $Ba_3TaFe_3Si_2O_{14}$ [16], $Ba_3NbFe_3Si_2O_{14}$ [17]).

Despite the fact that the magnetic ordering has been explained qualitatively, quantitative description of this phenomenon and, moreover, the problem of growing crystals with improved characteristics (elevated Neel temperature T_N) call for accumulation of structural data. Structural analysis shows that the calculation models of the magnetic interaction between atoms in langasite family crystals using geometric characteristics of atoms of only the average structure [6, 8] are simplified. One would expect the consideration of the atomic "spread" along the helix line to yield a larger value for the magnetic interaction. In addition, structural data of sufficient accuracy have been published for only two compounds with magnetic ions [16, 17]. The first purpose of our study was to develop a relatively precise and reproducible model of the atomic structure of SNFS crystal and analyze possible local atomic disorder.

A study of the thermal expansion of crystals with magnetic ions, $Ba_3NbFe_3Si_2O_{14}$ [17] and $Ba_3TaFe_3Si_2O_{14}$ [18], revealed an interesting effect. Upon cooling, the compression factor along the *c* axis in these crystals was found to be larger by a factor of 1.5–3 than along the *a* axis, whereas in langasite family crystals free of iron, in contrast, the compression factor along the *a* axis exceeded that along the *c* axis by a factor of 1.5–3. One can suggest this anomaly to be related to the influence of magnetic ions on the structural helix geometry: cooling reduces the average interatomic distance and provides conditions for stronger interaction between magnetic ions and compression of the helix along the *c* axis. For example, the helix compression upon cooling from room to liquid nitrogen temperature was found to be 0.0049 Å for $Ba_3TaGa_3Si_2O_{14}$ crystal [19] and 0.0072 Å for its iron-containing analog, $Ba_3TaFe_3Si_2O_{14}$ [18].

The magnetovolume effects and thermal expansion anomalies caused by magnetostriction are important both from the fundamental point of view (explanation of the nature of magnetism in solids) and in practical applications (design of temperature-compensated devices, whose geometry does not change as a result of thermal expansion; primarily, semiconductor and laser ones) [20]. Thus, the second purpose of our study was to analyze the thermal expansion of SNFS crystal, with development of the corresponding technique and software.

EXPERIMENTAL

Growth Technique of $Sr_3NbFe_3Si_2O_{14}$ Single Crystals

Czochralski growth of iron-containing langasites, in contrast to the growth of classical langasites by the same method [2, 21], meets serious difficulties. This is related to the more pronounced incongruent character of melting of iron-containing langasites in comparison with classical ones. The exact phase diagram of these compounds is unknown, as well as the existence of their congruently melting composition. Since iron-containing langasites have a component with a variable valence (iron oxide), the gas medium in the growth zone must be controlled during crystal growth from melt. Therefore, floating zone melting may be more efficient for growing these crystals. In this study, iron-containing langasite single crystals were grown by floating zone melting in a modified URN-2-ZP light-heating system [22]. To increase the density of a polycrystalline workpiece prepared by ceramic technology, it was remelted by zone melting at a rate of 35 mm/h in air. This preliminary operation improved the smoothness of workpiece melting and made the main growth process more stable. Growth was performed onto a seed cut from a single crystal, previously grown on a polycrystalline seed. The growth rate was 2–4 mm/h. The crystal and workpiece rotational speeds were, respectively, 20 and 1 rpm. The oxygen pressure above the melt in the crystallization chamber was chosen to be 10 atm. As-grown crystals were annealed at a temperature of 1200°C for 2 h in the growth chamber. When the growth was finished, the annealing temperature was gradually (for 5 h) reduced to room temperature. The thus obtained single crystals had a cylindrical shape with a diameter of 5–6 mm and a length of 40–50 mm. The crystal orientation was [111] or [110] along the boule axis. The boule had slightly faceting, an indication of good quality of crystal grown. Plates cut from the crystal (less than 0.5 mm thick) had red-orange color.

Primary quality control of the grown single crystals was performed by the Laue method using a digital XR NTX Laue Photonic Science instrument. Figure 2 shows a Laue pattern of SNFS crystal. No variations in Laue patterns were found when scanning boule cuts in the transverse and longitudinal directions. Phase analysis of the powder on a digital DRON-3 M diffractometer revealed no second-phase inclusions.

X-Ray Diffraction Experiment

The sample for diffraction analysis was rolled into an ellipsoid, whose shape was close to a sphere with a diameter less than 0.3 mm (Fig. 3). Four diffraction experiments were performed on an Xcalibur S diffrac-

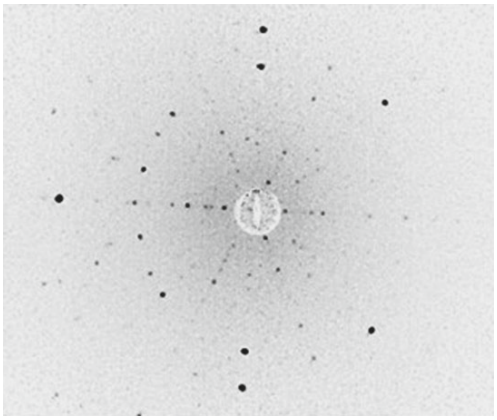

Fig. 2. Laue pattern of the $Sr_3NbFe_3Si_2O_{14}$ single crystal in the [110] direction.

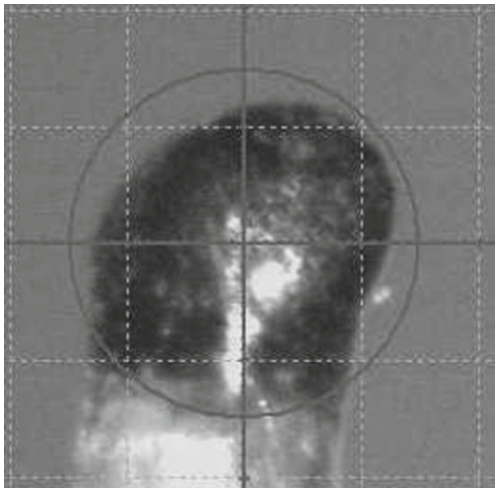

Fig. 3. Bright-field image of the sample; the circle diameter is 0.3 mm and the mesh spacing is 0.01 mm.

tometer (Rigaku Oxford Diffraction) with a CCD area detector at room temperature and at liquid nitrogen vapor temperature. To compensate for the systematic error, two data sets were measured at different sample orientations for each temperature. The sample was cooled using a Cobra Plus cryosystem (Oxford Cryosystems) with open cold nitrogen flow, directed onto the sample. A calibration carried out in [23] showed that the real sample temperature was 90.5 K in low-temperature measurements (82 K, according to the built-in sensor data) and 293 K at room temperature. The details of the X-ray experiment and parameters of the SNFS crystal structure refinement are listed in Table 1. The crystallographic data on the structures studied were deposited with the Inorganic Crystal Structure Database (ICSD) (CSD nos. 432883 and 432884).

The integral intensities were calculated from the diffraction patterns using the CrysAlis software [24]. The following data processing techniques (ASTRA software [25]) were applied: correction to the thermal diffuse scattering [26], correction of intensities to the radiation absorption for ellipsoidal samples [27], diffractometer calibration [28, 29], consideration of the extinction effect [30, 31], refinement of the half-wavelength contribution [32], the anharmonic displacement expert (automatic Hamilton–Fisher test) [25, 33], and the Abrahams–Keve test [34] for comparing models (normal probability plot). The final structural model was refined based on the cross-set obtained by averaging measurement results from two data sets (intermeasurement minimization or experimental comparison method) [35]. In the final stage, the refinement of models was repeated based on the measurements performed in individual experiments (Table 1) but using the data reduction, which was found when constructing a cross-set by the intermeasurement minimization method. The structural model of SNFS crystal was refined using squared moduli of structure factors, $|F|^2$. Friedel pairs were averaged, and the values of atomic-scattering factors were taken from [36]. The reliability of anharmonic models was verified by plotting the probability density function for electrons finding in a given volume of space and the Fourier difference maps. The Jana2006 program [37] was applied to this end.

To determine the thermal expansion of crystals, a special measurement technique was developed and a program for processing the results of multitemperature experiments was written. The values of the unit-cell parameters of crystals, obtained on diffractometers with area or linear detectors, are distorted by significant systematic errors. The reproducibility of the unit-cell parameters for approximately 20 langasite family crystals, determined on an Xcalibur S3 CCD diffractometer (Rigaku Oxford Diffraction), is worse by a factor of about 10 than the relative precision of the parameters found by the least-squares method in each individual experiment [10]. As a result, the temperature dependences of unit-cell parameters are nonmonotonic even in the temperature ranges without phase transitions and, correspondingly, difficult to interpret.

The following procedures were applied to overcome this hindrance. First, the measurements covered regions uniformly distributed in the reciprocal space, by analogy with the lists of the reflections used to refine the unit-cell parameters on point-detector diffractometers. Second, experiments were repeated from 4 to 8 times at each point, and their results were averaged.

RESULTS AND DISCUSSION

Based on the refinement results, the crystal under study was found to exist in one of the two possible enantiomorphic configurations, specifically, in the

Table 1. Crystallographic characteristics, experimental details, and parameters of the refinement for the $Sr_3NbFe_3Si_2O_{14}$ crystal structure model

Experiment	I	II	III	IV
T, K	293	293	90.5	90.5
Sample sizes in optical microscope, mm	0.22–0.28			
Calculated sample sizes, mm	0.210(1), 0.261(1), 0.279(1)	0.210(1), 0.256(1), 0.277(1)	0.195(1), 0.262(1), 0.311(1)	0.206(1), 0.256(1), 0.272(1)
System, sp. gr., Z	Trigonal, $P321$, 1			
a, c, Å	8.26069(7), 5.13148(5)	8.26119(6), 5.13110(5)	8.23482(5), 5.12467(4)	8.23399(5), 5.12390(5)
c/a	0.62119	0.62111	0.62232	0.62229
V, Å^3	303.254(5)	303.268(4)	300.957(3)	300.851(4)
μ, mm^{-1}	17.77		17.90	
α*, K^{-1}	$\|a$: 1.35×10^{-5}; $\|c$: 0.95×10^{-5}			
Diffractometer	Xcalibur S			
Radiation; λ, Å	MoK_α; 0.71073			
θ_{max}, deg	73.8	73.8	73.7	73.7
Ranges of indices h, k, l	$-21 \le h \le 20$, $-21 \le k \le 22$, $-12 \le l \le 13$	$-21 \le h \le 20$, $-21 \le k \le 22$, $-12 \le l \le 13$	$-21 \le h \le 20$, $-21 \le k \le 22$, $-12 \le l \le 13$	$-21 \le h \le 20$, $-21 \le k \le 22$, $-12 \le l \le 13$
Number of reflections: measured/unique with $F^2 \ge 2\sigma(F^2)$	31202/3480	31305/3541	31121/3537	31165/3582
Number of rejected unique reflections, $F^2 < 2\sigma(F^2)$	514	444	406	399
Redundancy	7.59	7.64	7.61	7.62
$\langle\sigma(F^2)/F^2\rangle$	0.051	0.049	0.047	0.047
$R1_{av}(F^2)/wR2_{av}(F^2)$, %	3.17/5.65	2.90/3.89	3.71/5.49	3.73/5.58
Number of parameters refined	90	90	85	85
$R1(\|F\|)/wR2(\|F\|)$, %	1.291/1.115	1.284/1.123	1.292/1.282	1.299/1.260
S	1.058	1.022	1.005	1.012
$\Delta\rho_{min}/\Delta\rho_{max}$, e/Å^3	−0.47/0.39	−0.39/0.38	−0.63/0.32	−0.75/0.34
Refinement based on the cross sets				
Number of reflections and parameters	3583/85		3638/78	
$R12_{av}(\|F\|)/wR12_{av}(\|F\|)$, %	1.261/0.907		1.211/0.947	
$R1(\|F\|)/wR2(\|F\|)$, %	1.175/1.031		1.183/1.127	
S	0.915		1.027	
$\Delta\rho_{min}/\Delta\rho_{max}$, e/Å^3	−0.57/0.25		−0.54/0.23	

Software in use: CrysAlis [24], ASTRA [25], and Jana2006 [37]. $\langle a\rangle$ = 8.2609(4) Å, $\langle c\rangle$ = 5.1313(3) Å at 293 K; $\langle a\rangle$ = 8.2344(6) Å, $\langle c\rangle$ = 5.1243(5) Å at 90.5 K; *α = $(1/\langle p\rangle)(\Delta p/\Delta T)$ is the thermal expansion coefficient in the temperature range ΔT = 90–293 K, p is the unit-cell parameter (a or c); $R12_{av}$ is the R factor for averaging identical reflections from two data sets on merging into a cross set; $R1(|F|) = \Sigma\||F_{obs}| - |F_{calc}|\|/\Sigma|F_{obs}|$; $wR2(|F|) = \sqrt{\{\Sigma w(|F_{obs}| - |F_{calc}|)^2/\Sigma w(F_{obs})^2\}}$.

right-handed (in the terminology of [38]) single-domain configuration; the Flack parameter [39] was close to zero: 0.008(2).

The refinement of the standard model of spherical atoms in the harmonic approximation, which includes 39 parameters, was finished with rather high reliability factors, and pronounced residual peaks were found in the difference electron-density map near atoms. This pattern is especially pronounced for the low-temperature experiment: $R1(|F|)/wR2(|F|)$ = 2.457/3.723%

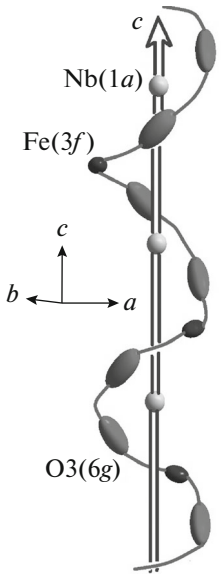

Fig. 4. Helical twist of the electron density of atoms in the chain of indirect exchange interaction Fe(3*f*)–O3(6*g*)–O3(6*g*)–Fe(3*f*) along the *c* axis of the $Sr_3NbFe_3Si_2O_{14}$ crystal, the helix axis passes through the Nb(1*a*) atom.

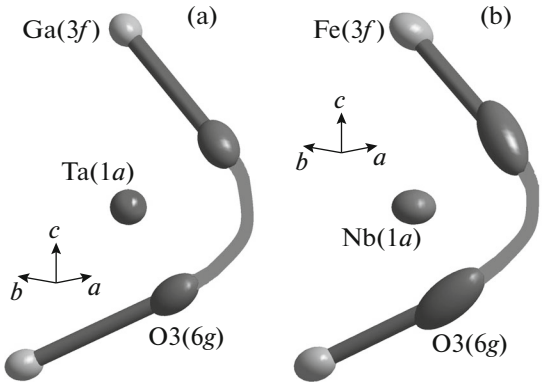

Fig. 5. Fragment of the electron density helix imitating the threefold screw symmetry axis in langasite family crystals: (a) moderate "spread" along the helix line in the $Ba_3TaGa_3Si_2O_{14}$ crystal and (b) strong "spread" in the iron-containing $Sr_3NbFe_3Si_2O_{14}$ crystal.

and $\Delta\rho_{min}/\Delta\rho_{max} = -2.74/2.79$ e/Å^3. The observed disordering of atomic sites in the SNFS structure was described within the model of anharmonic atomic displacements [40, 41]. The "anharmonic displacement expert" [42] indicated the atoms for which the anharmonic component was significant. According to the labeling introduced in [43], the models were denoted as 4232234 and 3442224 at 293 and 90.5 K, respectively. In other words, the anharmonic tensors describe the atomic displacements in the 3*e*, 3*f*, O2(6*g*), and O3(6*g*) sites at 293 K and in the 3*e*, 1*a*, 3*f*, and O3(6*g*) sites at 90.5 K. The transition to anharmonic models was accompanied by a twofold decrease in the reliability factors during the model refinement and "purification" of the Fourier difference maps (Table 1). Then we applied the "parameter significance expert" [42], due to which the number of refined parameters was reduced from 90 to 85 for the experiment at 293 K and from 85 to 78 for the experiment at 90.5 K. The refinement criteria were significantly improved after expanding the model: $R1(|F|) \sim 1.3\%$ and $\Delta\rho_{min}/\Delta\rho_{max} \sim -0.6/0.3$ e/Å^3 (at 90.5 K).

The atomic disordering asymmetry in the SNFS crystal was found to be most pronounced for the Fe(3*f*) site among cations and the O3(6*g*) site among anions. This leads to a pronounced helical twist of electron density with an axis passing through the Nb(1*a*) atom along the cell *c* axis (Fig. 4). The "spread" of the electron density along the helix line becomes especially pronounced in SNFS when comparing with crystals without magnetic ions, for example, $Ba_3TaGa_3Si_2O_{14}$ [19], CSD code no. 380523 in the ICSD database (Fig. 5). The found helix provides crystal chirality [9, 10] and serves as a base to form a magnetic helix at low temperatures [44].

The final structural models, presented in Tables 2 and 3, were refined according to the cross-sets obtained by averaging measurements from two data sets using the intermeasurement minimization method [35]. The estimation of the equivalent thermal parameters U_{eq} was supplemented by the calculation of the degree of elongation of thermal ellipsoids (ellipsoidality), which is given by the formula $\varepsilon = \sqrt{\{[(a-R)^2 + (b-R)^2 + (c-R)^2]/2\}}$, where *a*, *b*, and *c* are the principal semiaxes of thermal ellipsoid, and *R* is the radius of equivolume sphere (Table 2). The maximum difference between the model parameters obtained by refining models I and II (experiments I and II at 293 K in Table 1) is 2.5σ; at 90.5 K (experiments III and IV), this difference amounts to 5.4σ.

The structural transformation occurring upon cooling from 293 to 90.5 K manifests itself (along with the evident decrease in atomic displacement parameters, see Fig. 6) in the motions and significant increase in the ellipsoidality (Table 2) of the Fe(3*f*) and O3(6*g*) atoms, which form the structural helix, and in the displacement of the Sr(3*e*) atom from the origin of coordinates to the right (towards the cavity) (Fig. 1). The atom in the 3*e* site in langasite family crystals is fairly mobile along the *a* axis of the unit cell; the displacement of this atom by 70–80% determines the value of the piezoelectric coefficient e_{11} [45, 46]. Since the displacement of the 3*e* atom was observed in many crystals [9, 10], it was not unexpected in SNFS. A significant displacement of the cation in the 3*f* site upon cooling was observed in iron-containing $Ba_3NbFe_3Si_2O_{14}$ [17]. The mobility of Fe(3*f*) and O3(6*g*) atoms may indicate enhancement of the interatomic interaction caused by magnetic forces.

Table 2. Atomic coordinates, site occupancies Q, equivalent thermal parameters U_{eq}, and ellipsoidality of atomic displacements ε in the $Sr_3NbFe_3Si_2O_{14}$ crystal at 293 K (upper row) and 90.5 K (lower row)

Atom	Site	*x/a*	*y/b*	*z/c*	*Q*	U_{eq}, Å^2	ε
Sr	3*e*	0.43287(2) 0.43354(1)	0	0	1.0	0.01204(4) 0.00818(1)	0.0054 0.0039
Nb	1*a*	0	0	0	1.0	0.0125(1) 0.01013(8)	0.0130 0.0058
Fe	3*f*	0.75576(2) 0.75844(3)	0	1/2	1.0	0.01289(9) 0.0107(2)	0.0163 0.0204*
Si	2*d*	1/3	2/3	0.53571(6) 0.53574(5)	1.0	0.0101(3) 0.0084(4)	0.0063 0.0134
O1	2*d*	1/3	2/3	0.2241(1) 0.2233(1)	1.0	0.0146(4) 0.0099(5)	0.0200 0.0169
O2	6*g*	0.47328(7) 0.47283(6)	0.3074(1) 0.30717(7)	0.3345(2) 0.33295(8)	1.0	0.0165(1) 0.0121(1)	0.0280 0.0222
O3	6*g*	0.2172(2) 0.2162(1)	0.0830(2) 0.0783(2)	0.7658(2) 0.7624(2)	1.0	0.0262(3) 0.0288(3)	0.0611 0.0807*

* The increase in the ellipsoidality of Fe(3*f*) and O3(6*g*) atoms upon cooling is indicative of their stronger disordering along the structural (magnetic) helix line.

Table 3. Characteristics of atomic displacements U_{ij} (Å^2) in $Sr_3NbFe_3Si_2O_{14}$ crystal at 293 K (upper row) and 90.5 K (lower row)

Атом	U_{11}	U_{22}	U_{33}	U_{12}	U_{13}	U_{23}
Sr	0.01285(3) 0.00788(1)	0.01232(5) 0.00786(2)	0.01077(4) 0.00879(2)	0.00616(2) 0.003928(9)	−0.00009(1) 0.000242(8)	−0.00018(4) 0.00048(2)
Nb	0.01412(2) 0.00945(6)	0.0141(3) 0.0094(1)	0.00931(4) 0.0115(1)	0.0071(3) 0.0047(1)	0.0 	0.0
Fe	0.01323(2) 0.01060(3)	0.01435(3) 0.01482(9)	0.01145(3) 0.00802(8)	0.0072(3) 0.0074(4)	−0.00168(1) −0.00117(2)	−0.0034(2) −0.0023(3)
Si	0.01077(4) 0.00970(5)	0.0108(5) 0.0097(7)	0.00863(7) 0.00568(7)	0.0054(5) 0.0049(7)	0.0 	0.0
O1	0.0172(1) 0.0117(1)	0.0172(6) 0.0117(8)	0.0094(2) 0.0063(2)	0.0086(7) 0.0059(9)	0.0 	0.0
O2	0.0128(1) 0.0111(1)	0.0221(2) 0.0165(1)	0.0150(1) 0.0089(1)	0.0091(2) 0.0072(1)	0.00022(9) 0.00021(9)	0.0044(1) 0.0025(1)
O3	0.0182(3) 0.0139(4)	0.0351(5) 0.0347(4)	0.0296(4) 0.0407(4)	0.0165(3) 0.0142(3)	0.0095(3) 0.0106(3)	0.0175(4) 0.0232(4)

The enhancement of the interaction along the helix line may lead to the helix compression along the cell *c* axis, i.e., to a significant decrease in the unit-cell parameter *c* in iron-containing langasite. This effect was observed in practice: the compression of the *c* axis in $Ba_3TaFe_3Si_2O_{14}$ and $Ba_3NbFe_3Si_2O_{14}$ crystals upon cooling is much larger than in their iron-free analogs. The thermal expansion in SNFS was found to be more complex (Fig. 7). If measurements were performed in the range of 150–293 K, the aforementioned strong compression along the *c* axis would be confirmed on the whole. However, anomalous negative thermal expansion ($\alpha = (1/\langle p \rangle)(\Delta p/\Delta T) = -0.532 \times 10^{-5}$ K^{-1}) along the cell *c* axis was observed in the range of 83–110 K, and the compression along the *c* axis in the range of 83–293 K was found to be somewhat weaker than along the *a* axis (Table 1).

From the thermodynamic point of view, the anomaly of negative thermal expansion indicates an unexpected increase in the entropy of the system with a decrease in temperature [47], which was detected in structural analysis as an increase in the degree of structural disordering of atoms upon cooling to 90.5 K. This behavior can be considered as a precursor of the $P321 \rightarrow P3$ phase transition, which existence is related to magnetic ordering [8]; however, this transi-

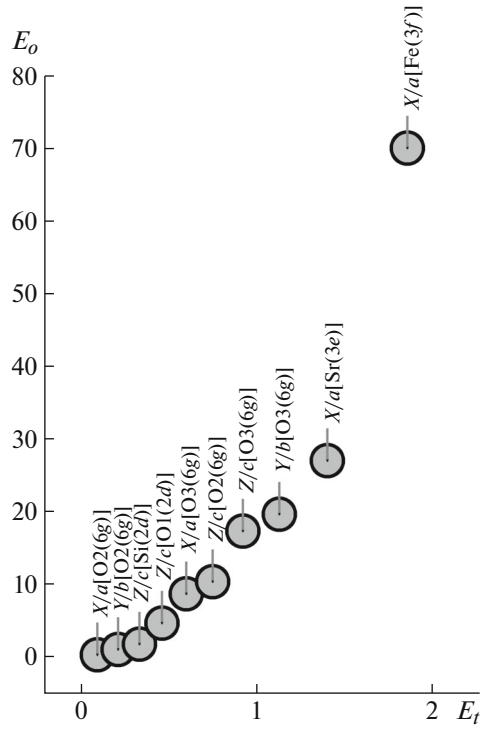

Fig. 6. Comparison of the atomic coordinates in the $Sr_3NbFe_3Si_2O_{14}$ crystal at 293 and 90.5 K on the normal probability plot; E_t and E_o are, respectively, the theoretical and experimental errors. The most mobile atom is Fe(3*f*).

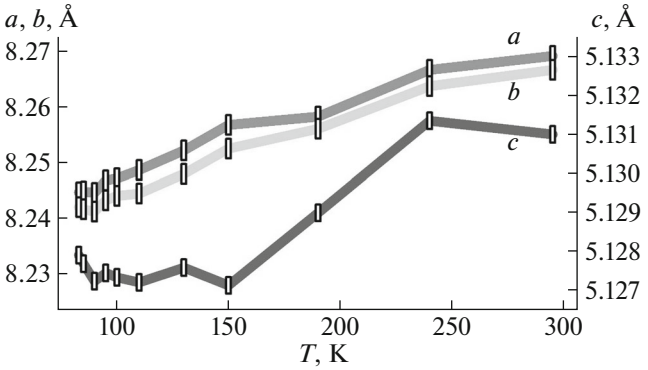

Fig. 7. Temperature dependences of the unit-cell parameters of $Sr_3NbFe_3Si_2O_{14}$ crystal. Ranges of anomalous negative thermal expansion are fixed for the parameter *c*.

tion has not been detected to date. As a result of the phase transition, magnetic ions Fe(3*f*) should leave the twofold symmetry axis, a circumstance facilitating the alignment of their spins along the helix line. A helium-temperature study is being planned in order to detect this phase transition and analyze more thoroughly the negative thermal expansion.

CONCLUSIONS

An X-ray diffraction study of the $Sr_3NbFe_3Si_2O_{14}$ crystal was performed using averaged data sets obtained at two temperatures: sp. gr. *P*321, $Z = 1$, $\sin\theta/\lambda \le 1.35$ Å^{-1}; $a = 8.2609(4)$ Å, $c = 5.1313(3)$ Å at 293 K and $a = 8.2344(6)$ Å, $c = 5.1243(6)$ Å at 90.5 K; agreement factors $R/wR = 1.18/1.03\%$ and $\Delta\rho_{min}/\Delta\rho_{max} = -0.57/0.25$ e/Å^3 for 85 refined parameters and 3583 independent reflections at 293 K and $R/wR = 1.18/1.13\%$ and $\Delta\rho_{min}/\Delta\rho_{max} = -0.54/0.23$ e/Å^3 for 78 refined parameters and 3638 reflections at 90.5 K. A satisfactory reproducibility of results was obtained in repeated experiments: the maximum difference between the model parameters is 2.5σ and 5.4σ at 293 and 90.5 K, respectively. The crystal structure is described within the anharmonic model, which shows disorder of the atomic structure; i.e., one observes displacement of time-averaged atomic coordinates from the lattice sites. This displacement increases upon cooling, which may indicate a tendency to static splitting of atomic sites, despite the fact that each site in the crystal is occupied by similar atoms. The structural results are in agreement with the NMR and Mossbauer spectroscopy data on langasite family crystals, which are indicative of wide distribution of local atomic environments [14] and splitting of atomic sites [5]. In the range of 83–110 K, an anomalous negative thermal expansion ($\alpha = -0.532 \times 10^{-5}$ K^{-1}) along the cell *c* axis was found; this feature may be a precursor of the $P321 \rightarrow P3$ phase transition.

ACKNOWLEDGMENTS

The structural part of the work was performed within research project no. 0026-2014-0001 (“Development and Application of Diagnostic Methods for Inorganic, Organic, and Bioorganic Materials Using X Rays, Synchrotron Radiation, Electrons, and Neutrons”) on the equipment of the Shared Equipment Center of the Shubnikov Institute of Crystallography, Federal Scientific Research Centre “Crystallography and Photonics,” Russian Academy of Sciences, and supported in part by the Ministry of Education and Science of the Russian Federation (project RFMEFI62114X0005), the Russian Foundation for Basic Research (project no. 14-02-00531), and State contract no. 872.

REFERENCES

1. E. L. Belokoneva and N. V. Belov, Dokl. Akad. Nauk SSSR, **260** (6), 1363 (1981).
2. B. V. Mill and Yu. V. Pisarevsky, *Proc. IEEE/EIA Intern. Frequency Control Symp., Kansas City, Missouru, USA, 2000,* p. 133.
3. V. Yu. Ivanov, A. A. Mukhin, A. S. Prokhorov, and B. V. Mill, Solid State Phenom. **152–153**, 299 (2009).
4. H. D. Zhou, L. L. Lumata, P. L. Kuhns, et al., Chem. Mater. **21**, 156 (2009).

5. I. S. Lyubutin, P. G. Naumov, B. V. Mill', et al., Phys. Rev. B **84**, 214425 (2011).
6. S. A. Pikin and I. S. Lyubutin, Phys. Rev. B **86**, 4414 (2012).
7. H. Narita, Y. Tokunaga, A. Kikkawa, et al., Phys. Rev. B **94**, 094433 (2016).
8. K. Marty, P. Bordet, V. Simonet, et al., Phys. Rev. B **81**, 054416 (2010).
9. A. P. Dudka and B. V. Mill', Crystallogr. Rep. **58** (4), 594 (2013).
10. A. P. Dudka and B. V. Mill', Crystallogr. Rep. **59** (5), 689 (2014).
11. A. P. Dudka, Crystallogr. Rep. **62** (2), 195 (2017).
12. A. P. Dudka, Crystallogr. Rep. **62** (3), 374 (2017).
13. I. S. Lyubutin, P. G. Naumov, and B. V. Mill, Europhys. Lett. **90**, 67005 (2010).
14. A. Zorko, F. Bert, P. Bordet, et al., J. Phys.: Conf. Ser. **145**, 012006 (2009).
15. A. P. Dudka, Crystallogr. Rep. **61** (2), 187 (2016).
16. A. P. Dudka, A. M. Balbashov, and I. S. Lyubutin, Crystallogr. Rep. **61** (1), 24 (2016).
17. A. R. Dudka, A. V. Balbashov, and I. S. Lyubutin, Cryst. Growth Des. **16**, 4943 (2016).
18. A. P. Dudka and A. M. Balbashov, *Fifth European Conference on Crystal Growth (ECCG5), Bologna, Italy, September 9–11, 2015,* p. S11.
19. A. P. Dudka, *Proc. VIII National Crystallochemical Conference, Suzdal', May 30–June 3, 2016,* p. 129.
20. K. Takenaka, Sci. Technol. Adv. Mater. **13**, 013001 (2012).
21. S. Uda, S. Q. Wang, N. Konishi, et al., J. Cryst. Growth **237–239**, 707 (2002).
22. A. M. Balbashov and S. K. Egorov, J. Cryst. Growth **52**, 498 (1981).
23. A. P. Dudka, I. A. Verin, and E. S. Smirnova, Crystallogr. Rep. **61** (4), 692 (2016).
24. Agilent Technologies, *Xcalibur CCD System, CrysAlisPro Software System, Version 1.171.35 21* (Agilent Technologies, Oxford, UK, 2011).
25. A. Dudka, J. Appl. Crystallogr. **40**, 602 (2007).
26. A. P. Dudka, M. Kh. Rabadanov, and A. A. Loshmanov, Sov. Phys. Crystallogr. **34** (4), (1989).
27. A. P. Dudka, Crystallogr. Rep. **50** (6), 1068 (2005).
28. A. Dudka, J. Appl. Crystallogr. **43** (6), 1440 (2010).
29. A. P. Dudka, Crystallogr. Rep. **60** (4), 601 (2015).
30. P. J. Becker and P. Coppens, Acta Crystallogr. A **30**, 129 (1974).
31. Y. Le Page and E. J. Gabe, J. Appl. Crystallogr. **11**, 254 (1978).
32. A. Dudka, J. Appl. Crystallogr. **43**, 27 (2010).
33. W. C. Hamilton, Acta Crystallogr. **18**, 502 (1965).
34. S. C. Abrahams and E. T. Keve, Acta Crystallogr. A **27**, 157 (1971).
35. A. P. Dudka, Crystallogr. Rep. **47** (1), 152 (2002).
36. Z. Su and P. Coppens, Acta Crystallogr. A **54**, 646 (1998).
37. V. Petricek, M. Dusek, and L. Palatinus, Z. Kristallogr. **229** (5), 345 (2014).
38. V. N. Molchanov, B. A. Maksimov, D. F. Kondakov, et al., JETP Lett. **74** (4), 222 (2001).
39. H. D. Flack, Acta Crystallogr. A **39**, 876 (1983).
40. P. I. Kuznetsov, R. L. Stratonovich, and V. I. Tikhonov, Teor. Veroyatn. Ee Primen. **5** (1), 84 (1960).
41. C. K. Johnson, Acta Crystallogr. A **25**, 187 (1969).
42. A. P. Dudka, Crystallogr. Rep. **53** (2), 351 (2008).
43. A. P. Dudka and B. V. Mill', Crystallogr. Rep. **56** (3), 443 (2011).
44. S. A. Pikin, I. S. Lyubutin, and A. P. Dudka, Crystallogr. Rep. **60** (5), 729 (2015).
45. N. Araki, H. Oshato, K. Kakimoto, et al., J. Eur. Ceram. Soc. **27**, 4099 (2007).
46. A. P. Dudka and V. I. Simonov, Crystallogr. Rep. **56** (6), 980 (2011).
47. G. D. Barrera, J. A. O. Bruno, T. H. K. Barron, and N. L. Allan, J. Phys.: Condens. Matter **17**, R217 (2005).

Translated by Yu. Sin'kov